International Journal of Microwave and Wireless Technologies

cambridge.org/mrf

Coupling receiver–transmitter metasurface-based Fabry–Pérot resonant antenna with dual circular polarization

Zhiqiang Yuan

Physical Science and Technology College, Yichun University, Yichun, Jiangxi 336000, China

Research Paper

Cite this article: Yuan Z (2023). Coupling receiver–transmitter metasurface-based Fabry–Pérot resonant antenna with dual circular polarization. *International Journal of Microwave and Wireless Technologies* **15**, 881–890. https://doi.org/10.1017/S1759078722001027

Received: 12 May 2022
Revised: 31 August 2022
Accepted: 1 September 2022

Key words:
Aperture efficiency; circular polarization; Fabry–Pérot (FP); polarization conversion; RT-MS

Author for correspondence:
Zhiqiang Yuan,
E-mail: ycxy_yzq@126.com

Abstract

This study presents a dual-circularly polarized (CP) Fabry–Pérot (FP) antenna, employing a novel receiver–transmitter (RT) metasurface (MS). The RT-MS unit cell consists of two identical neighboring substrates, with a three-layer metal coating printed on their surfaces. The bottom patch is adopted as a receiver to transfer electromagnetic waves to the top-corner cut patch, passing through the coupling cross-slot sandwiched in the middle. The RT-MS has high reflectivity to achieve a high gain. Through energy and a cross-slot, high aperture efficiency can be realized. A conventional corner cut patch can excite a CP mode of equal magnitude and a 90° phase difference. The RT-MS is arranged in 12×12 unit cells and used as a superstrate for a dual-CP antenna. Two orthogonally etched slots fed by two branch-matched orthogonally arranged feed lines are used as feeders to produce perpendicular linearly polarized waves. To enhance the bandwidth and improve the gain, double identical stack substrate patches are placed at the top side of the slot with no air gap, for a wide impedance band and high gain. Two wide CP bands, left-hand circular polarization and right-hand circular polarization, of 12.21–13.1 GHz (7.03%) and 12.35–13.1 GHz (5.89%), respectively, have maximum high gains of 16.5 and 15.97 dBic at 12.58 and 12.7 GHz, respectively, with a compact size of $2.6\lambda_0 \times 2.6\lambda_0$, suggesting better properties than recent antennas. The aperture efficiency can reach 63.2%. Thus, the RT-MS-based FP antenna is a good candidate for commercial and military communication systems.

Introduction

Circularly polarized (CP) antennas play an important role in wireless communication systems and point-to-point links owing to their high tolerance to multi-path effects and polarization mismatching, so there is a high demand for CP antennas with properties such as a high gain, wideband, and a wide 3 dB axial ratio angle. CP antennas are designed by many methods. Among them, metasurfaces (MS) have proved to be efficient in CP generation and performance enhancement. Thus, a series of linear-to-circular polarization conversion MS-based antennas have been designed [1–8]. In previously reported MS-based antennas, slot source antennas were usually used as feeders for their wideband to produce linearly polarized (LP) waves, which could be generated after passing through a polarization conversion metasurface (PCM), a polarization conversion to the CP mode [1–4]. Owing to their high gain property, several Fabry–Pérot (FP) resonant cavity antennas have been proposed in the design of CP antennas [9–15]. A PCM array consisting of two neighboring metal-coating-substrate unit cells, which act as a superstrate and feeding slot antenna, was combined in an FP-CP antenna [1], realizing an enhanced gain and wideband CP radiation while maintaining a compact size. Another FP resonant cavity was formed by an all-metal cross-slot-etched frequency-selective surface and a nonstandard artificial magnetic conductor [16]. Fed by an obliquely placed patch, the antenna achieved high gain, wideband CP performance [17]. Other polarization-reconfigurable MS-based FP-CPs were also reported [18]. However, most CP-FP antennas can only realize either a left-hand circular polarization (LHCP) or right-hand circular polarization (RHCP) state, while the dual-CP mode can be applied in a wider range for flexible controlled polarization according to requirements. Following this, several FP-CP antennas were proposed [19–24]. As reported in related work, the dual-CP mode was realized in two ways: a dual-polarization source antenna acting as a feeder, and MSs, which convert to CP waves for LP signals at different frequencies, act as a superstrate. A polarization-reconfiguration source patch antenna, acting as a feeder, was proposed, where an MS-based FP antenna for LHCP, RHCP, and LP states can be realized by changing the polarization of the feeder [25]. Through the design of different responses for LP waves, an MS superstrate can convert LP waves to different CP waves at different frequencies, resulting in a dual-CP FP resonant antenna [26]. A dual-port slot source feeder was proposed to realize two polarization conversions when fed by different ports [27]. The above techniques do not consider size reduction,

high gain, and wideband, which pose a challenge to achieving satisfactory properties in a compact design.

The receiver–transmitter metasurface (RT-MS) suggests a possible FP cavity antenna with high reflectivity and low transmissivity, resulting in high gain [28, 29]. RT-MS generally consists of receiver and transmitter patches, along with a coupling layer. The incident wave is received by the bottom patch and coupled with the top patch [30, 31]. An off-center metal via a connecting receiver and transmitter was adopted to couple energy radiated by the slot antenna, resulting in a CP mode and achieving a high gain [32]. However, it can only operate in a single polarization working band, while the aperture efficiency has a possible enhancement. To easily realize the phase and magnitude of the transmission, a slot-coupling approach was adopted [33], which achieved a high aperture efficiency, which gives us a reference for MS design with high-aperture efficiency. Slot-coupling occurs in dual-polarization antenna design [27]. However, the gain-enhancement, resulting from the FP cavity, as well as the band improvement, has a possible increment, as shown through the design of a novel RT-MS and dual-feeder for the high gain property.

This study proposes a linear-to-circular polarized RT-MS of cross-slot coupling, with high gain, high aperture efficiency, and a dual-CP FP antenna. It has a rectangle patch as a receiver, a cross-slot coupling layer, and a corner-cut patch as a transmitter. The MS, with a transmission phase and magnitude-independent control, is designed to possess combined high reflectivity and the polarization conversion function, enabling the proposed antenna to achieve high gain and wide CP radiation. A dual-LP slot source antenna, acting as a feeder, produces LP waves, which can be operated independently. Thus, a high gain, high aperture efficiency, and a wide CP band FP resonant antenna are realized.

The remainder of this article is organized as follows. Section "Design process and analysis of proposed PCM" provides the design procedure and analysis of the proposed RT-PCM with high reflectivity and circular polarization conversion. Section "Analysis and design of proposed CP-FP antenna" presents the design and analysis of the FP-CP antenna. Section "Simulated and measured results" validates the design through simulated and measured results. We provide our conclusions in section "Conclusions".

Design process and analysis of proposed PCM

Generally, in a PCM-based antenna, an FP cavity is formed by a PCM and ground plane separated by a certain distance. As shown in Fig. 1, the electromagnetic wave illuminated by the radiator in the center of the cavity can be multiply reflected and transmitted into space.

To obtain the maximum directivity, reflected and re-reflected waves in the cavity must be transmitted in phase. Hence, as shown in (1), the reflection phases of the ground plane, ϕ_{GND}, and those of PCM, ϕ_{PCM}, should satisfy

$$\phi_{\mathrm{pcm}} + \phi_{\mathrm{GND}} - \frac{4\pi h_c}{\lambda_0} = 2N\pi, \quad N = 0, \ \pm 1, \ \pm 2 \ldots. \tag{1}$$

Hence, a separation distance, h_c, between them can be determined. Once the feeding antenna is designed, the center frequency and ϕ_{GND} are basically fixed; that is, by optimizing

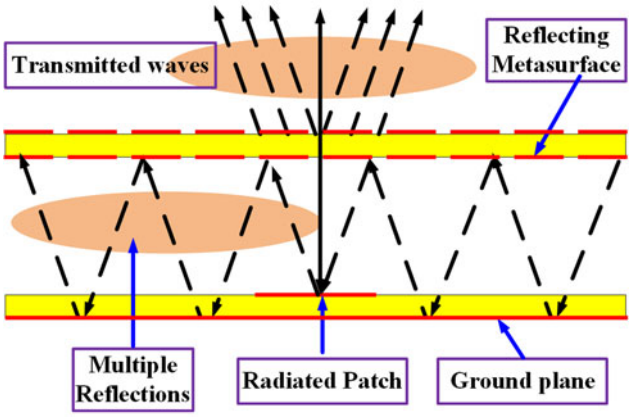

Fig. 1. Ray theory model of the Fabry–Pérot cavity antenna for increasing directivity.

ϕ_{PCM}, a relatively smaller resonance mode, N, can be selected, and a low profile can be obtained.

The boresight directivity of the antenna can be calculated as in [26]:

$$D_r = 10\log\frac{1+R}{1-R}, \tag{2}$$

where R is the reflection magnitude of the PCM. Thus, a higher directivity is generated when R is larger, with the maximum directivity occurring when R is around 0.9 [33].

Based on the above analysis, when designing a dual CP-FP resonant antenna, three requirements should be met. The reflectivity of the proposed PCM must be high enough to achieve a high gain. The transmission coming from the cavity for coefficients $T11$ and $T21$ should have a phase difference of 90°, and be of equal or almost equal magnitude, to be transformed from LP to CP. Note that we define $T11$ as the transmission coefficient of the transfer of x-polarized waves to x-polarized waves when passing through PCM. So $T21$ represents the transfer of x-polarized waves to y-polarized waves when passing through PCM, where polarization conversion is realized. Then, as a source antenna feeding the PCM, the two orthogonal linear polarizations should be independently controlled, with high isolation; that is, the two $S11$s have no or less mutual effect. Hence, we use the following design process.

As shown in Fig. 2, the unit cell is constructed from two identical neighboring substrates ($\varepsilon_r = 3.5$, $\tan\delta = 0.0014$, $h = 1.524$ mm) of the size 5 mm × 5 mm, with three metal patches printed on them, consisting of a rectangle on the bottom, a cross-slot in the middle, and a conventional corner-cutting on the top. Figure 2(e) shows an HFSS model, where an incident wave can be received by the bottom patch of the receiver, coupled with the cross-slot to the radiated patch of the transmitter, where a CP wave radiates into space.

We investigated the lengths of the receiver patch, W_a, and cross-slot, L_m, as shown in Fig. 3. It can be seen in Fig. 3(a) that a larger size is preferred for lower reflectivity, which decreases as W_a increases from 3.5 to 4.5 mm. However, there is little influence on the transmission, which remains at about 0.95, ensuring a high gain with high reflectivity, R. A larger reflectivity is obtained as the length of the cross-slot decreases. We set $W_a = 4$ mm and $L_m = 3$ mm to achieve a reflectivity of around 0.95, which ensures a high gain.

To introduce the cross-polarization component of transmission of the unit cell, the conventional technique of the corner

https://doi.org/10.1017/S1759078722001027 Published online by Cambridge University Press

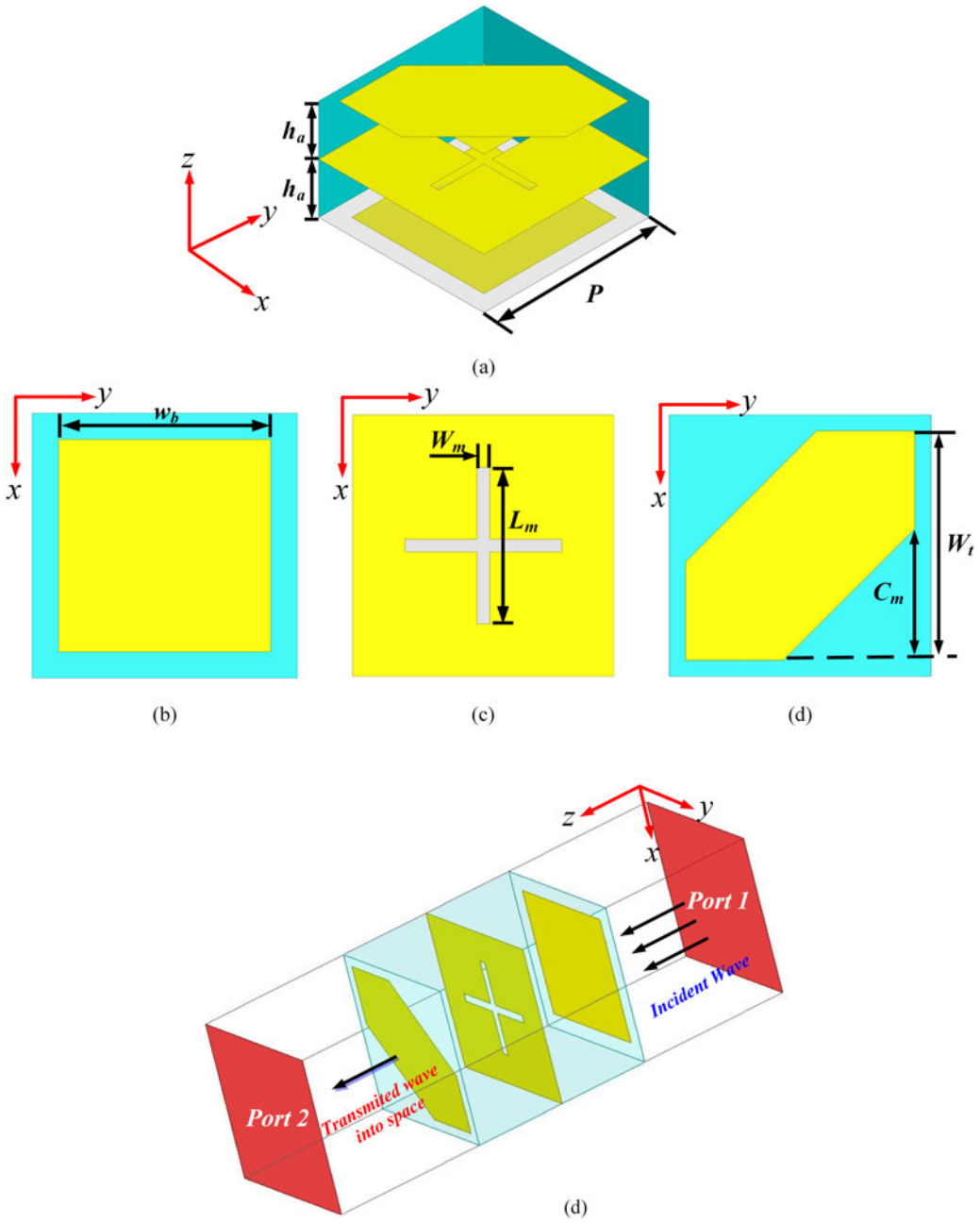

Fig. 2. Geometry of RT-MS unit cell. Detail views of the unit cell for three layers: (a) transmitter patch; (b) etched cross-slot coupling metal plane; (c) receiver patch; (d) simulated model of the unit cell in HFSS.

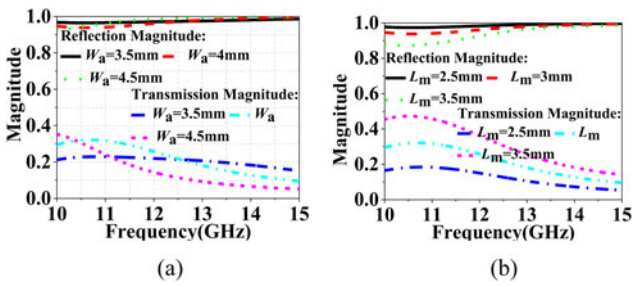

Fig. 3. Effect on *S* parameters at different lengths: (a) W_a; (b) L_m.

cut is applied for the transmission of equal magnitude and a 90° difference. As plotted in Fig. 4(b), a wideband of almost equal magnitude across 10–15 GHz is obtained. Then, when C_m is equal to 2.5 mm, a pure 90° difference phase, indicating a phase of *T*21 being ahead 90° of that of *T*11, which leads to an LHCP wave coming out of the cavity, is achieved, with a band of ranging from 11.5 to 13.5 GHz. The band has a 0.95 higher reflectivity simultaneously, as shown in Fig. 4(a). Thus, a LP to CP transform across a band of 11.5–13.5 GHz is achieved, demonstrating that the transmitter can radiate CP waves.

Figure 5 shows simulated *E*-field distributions for the horizontal and vertical linear polarization of the designed MS. When a horizontal linear polarization (HLP) wave is received, the coupling cross-slot can be motivated by the most *E*-field energy

https://doi.org/10.1017/S1759078722001027 Published online by Cambridge University Press

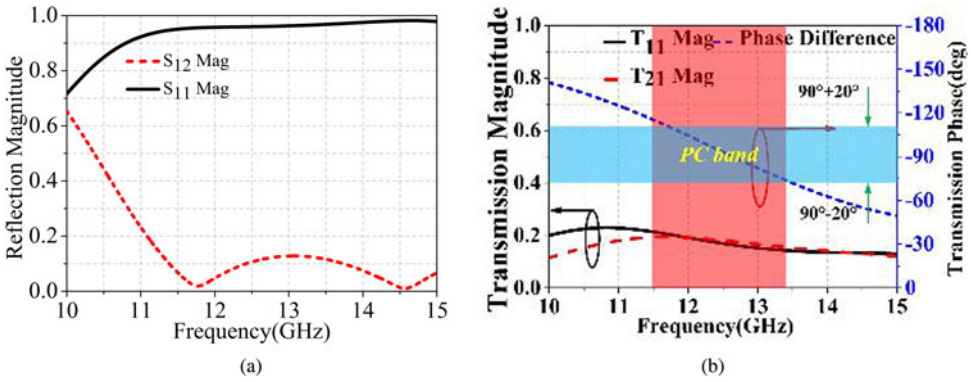

Fig. 4. Magnitudes and phases of transmission and reflection versus frequency for the optimum values granted to the unit cell: (a) magnitudes of reflection and transmission; (b) magnitude and phase difference for transmission.

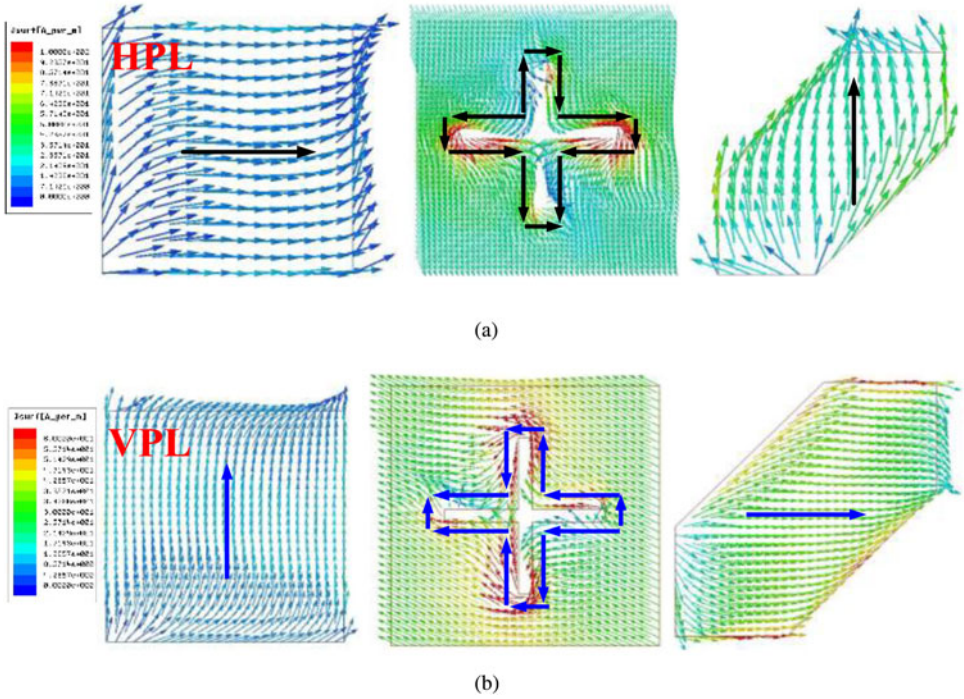

Fig. 5. Simulated *E*-field distributions for responses to different linearly polarized waves in three layers: (a) horizontal; (b) vertical.

concentrated on it to obtain a radiation of 90° counterclockwise of the LHCP. This is different from the radiated wave to the vertical linear polarization (VLP) wave of 90° clockwise of RHCP, suggesting that the MS can perform in HPL and VPL CP modes.

To explain the working principle, assuming illumination with a HLP wave, *E*-field distributions at the center plane of the cross-slot at 12.5 GHz in two orthogonal direction planes are given in Figs 6(a) and 6(b). The coupled electromagnetic wave passing through the cross-slot is roughly divided into two orthogonally distributed parts. The energy of the *E*-field is concentrated on the edge of the corner-cut radiated patch along the diagonals, with a 90° rotation. As displayed in Fig. 6(b), the *E*-field at another plane exhibits the same distributions, but the energy is obviously weak and can be ignored, demonstrating that the vertical branch of the cross-slot can only couple vertically polarized waves. This indicates that the cross-slot receives the wave from the receiver and is coupled with the transmitter with circular polarization.

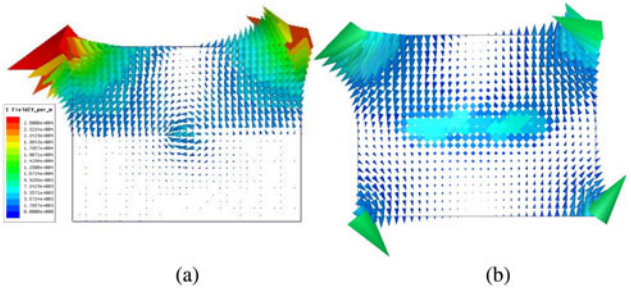

Fig. 6. Simulated *E*-field distributions at 12.5 GHz in two orthogonal planes: (a) *xoz* plane; (b) *yoz* plane.

Analysis and design of proposed CP-FP antenna

The proposed antenna is formed by a feeding antenna and PCM superstrate separated by an FP cavity. To guarantee a satisfactory gain property, a larger size is preferred to avoid wave diffraction at

https://doi.org/10.1017/S1759078722001027 Published online by Cambridge University Press

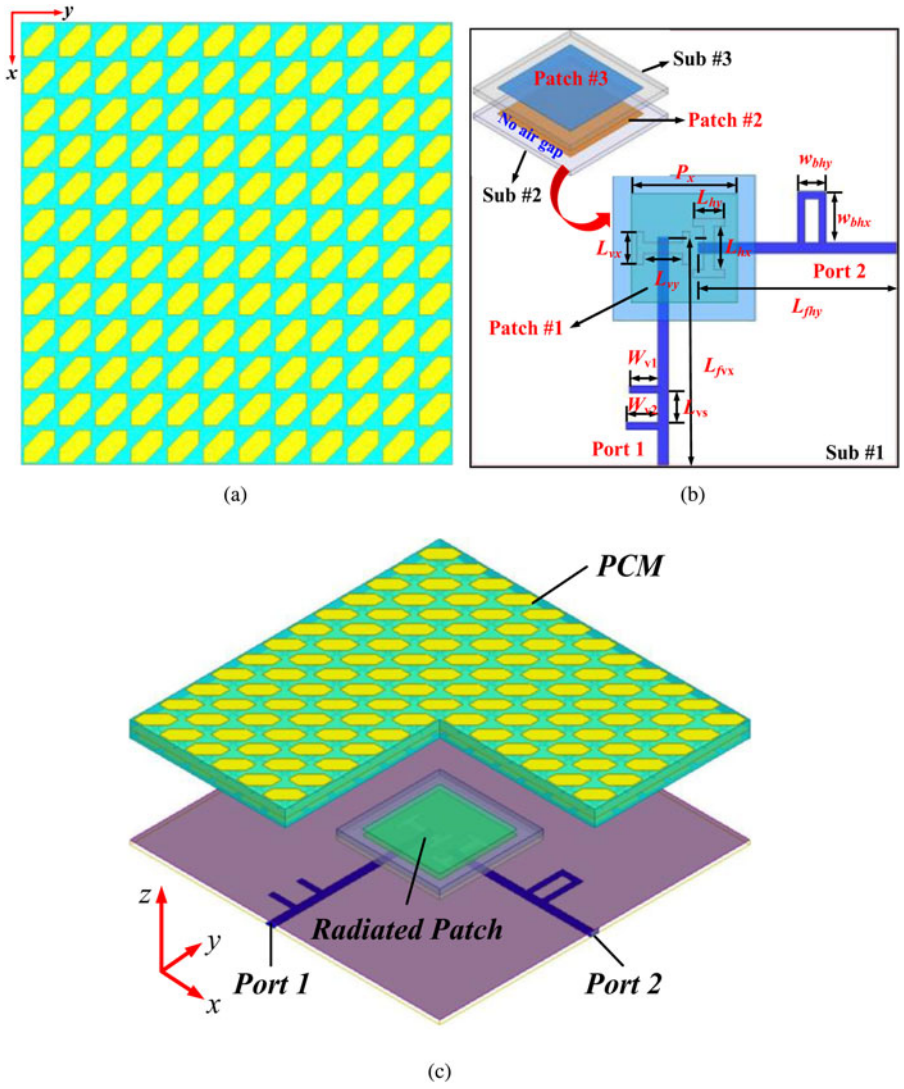

Fig. 7. Configuration of proposed dual-CP FP resonant antenna: (a) PCM; (b) sketch model of dual linear-polarization source feeding antenna and detailed views; (c) 3D sketch with dimensions $W_{v1} = 4$ mm, $W_{v2} = 4.5$ mm, $P_x = 15$ mm, $P_{sx} = 20$ mm, $L_{vx} = 4.5$ mm, $L_{vy} = 5.5$ mm, $L_{hx} = 4.5$ mm, $L_{hy} = 6$ mm, $L_{fhy} = 28$ mm, $L_{fvx} = 31.5$ mm, $W_{bhy} = 3$ mm, $L_{bhx} = 7$ mm, $L_{vs} = 4$ mm.

the edge of the cavity. However, owing to the small contribution in gain enhancement on the edge of the MS and less energy distributed on the cavity edge as the size increases, the aperture efficiency, that is,

$$\eta = G\frac{\lambda_0^2}{4\pi A}, \tag{3}$$

decreases, where G is the boreside gain, and A is the physical size of the aperture. Through numerical simulations, a tradeoff is made between gain and efficiency. Consequently, a $60\,\text{mm} \times 60\,\text{mm}$ PCM array with a 12×12 unit cell is formed, as shown in Fig. 7.

Table 1. Optimal dimensions of proposed RT-MS

Dimension	Size (mm)	Dimension	Size (mm)
h_a	1.524	p	5
w_a	4	w_t	4.375
w_m	0.25	C_m	2.5
L_m	3		

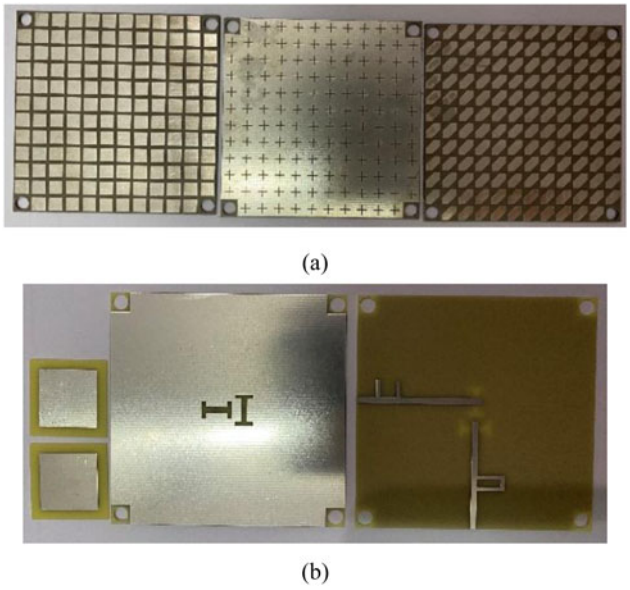

Fig. 8. Photograph of fabricated antenna: (a) PCM superstrate; (b) feeder.

https://doi.org/10.1017/S1759078722001027 Published online by Cambridge University Press

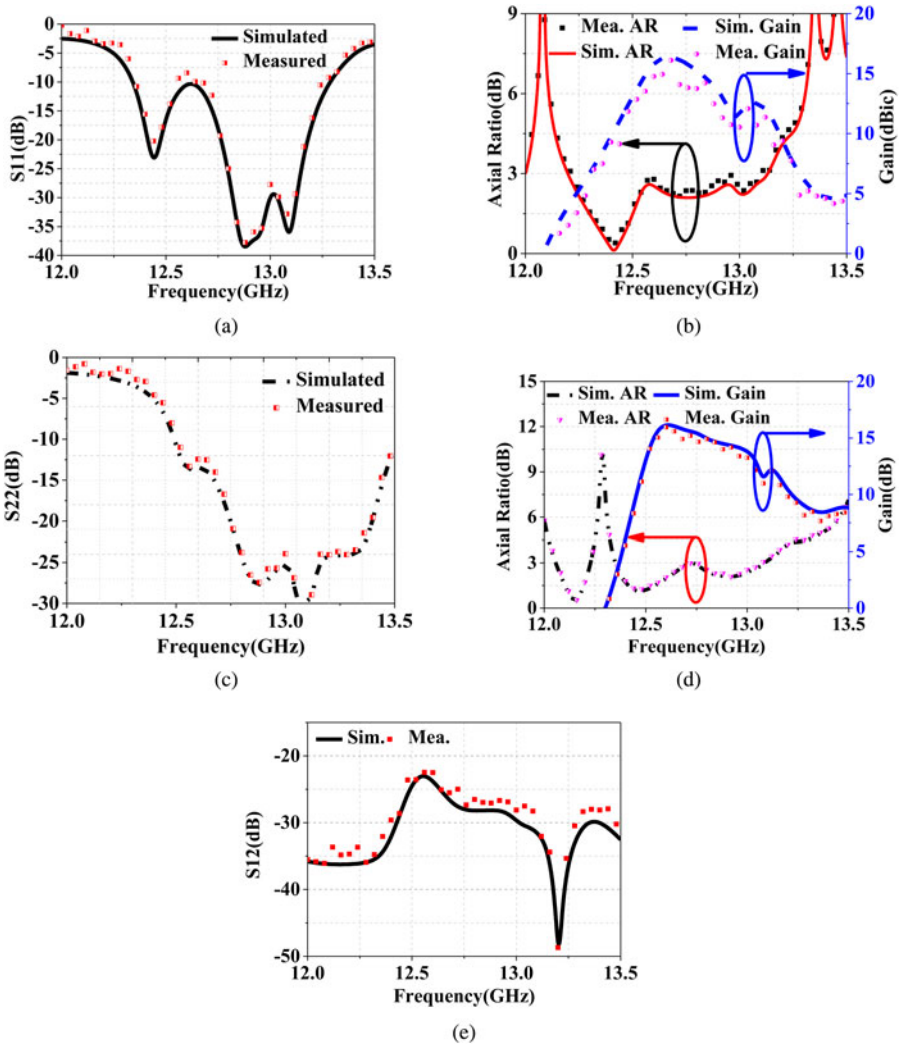

Fig. 9. Simulation and mensuration of proposed CP-FP antenna for port1 and port 2 under *x* and *y* incident waves. Results under *x* incident wave: (a) *S*11; (b) AR and bore-side gain. Results under *y* incident wave: (c) *S*22; (d) AR and bore-side gain; (e) *S*12.

To achieve dual-LP waves in one source antenna, dual etched *H*-shaped slots in a metal plane is adopted in this design. Thus, a flexible switching on the two polarizations can be obtained. Figure 7(b) displays the configuration of the dual-polarized feeding antenna, which consists of three stacked metal substrates with a non-uniform size: Sub #1, Sub #2, and Sub #3. Sub #1 is made of Rogers RT ($\varepsilon_r = 2.2$, $\tan\delta = 0.0014$), with a thickness of 1.6 mm. Sub #2 and Sub #3 are 20 mm × 20 mm, and are made of Rogers TMM4 ($\varepsilon_r = 4.4$, $\tan\delta = 0.0014$), with a thickness of 0.8 and 1 mm, respectively. Note that there are no air gaps between them. To improve the impedance matching, which is worsened by the strong resonance of FP, shunt stubs are applied, whose impedance, through tuning, can match well with a wider band-pass. Stacked patches at the top of Sub #1 and Sub #2 are used to enhance the broadside gain of the antenna. Two 50 ohm SMAs (SubMiniature version A) connect to the edge of the

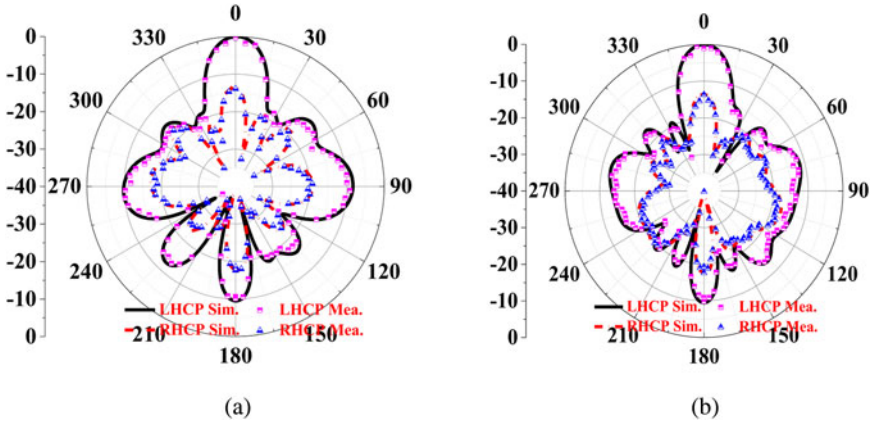

Fig. 10. Simulated and measured radiation pattern at 12.5 GHz fed by port1: (a) *xoz* plane; (b) *yoz* plane.

https://doi.org/10.1017/S1759078722001027 Published online by Cambridge University Press

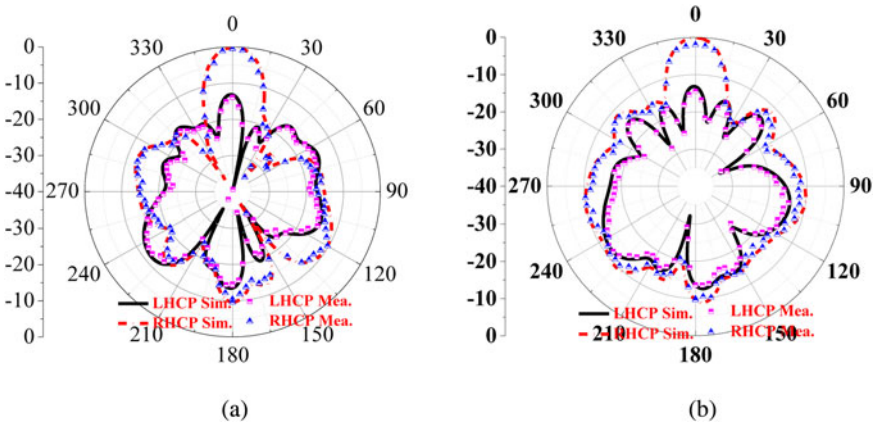

Fig. 11. Simulated and measured radiation pattern at 12.7 GHz fed by port2: (a) *xoz* plane; (b) *yoz* plane.

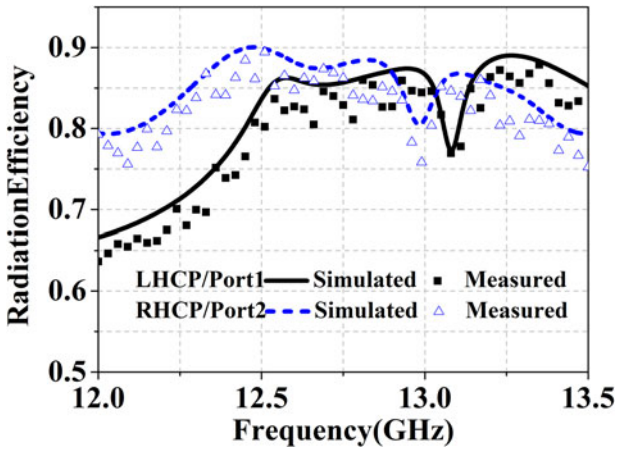

Fig. 12. Simulated radiation efficiency for LHCP and RHCP radiation.

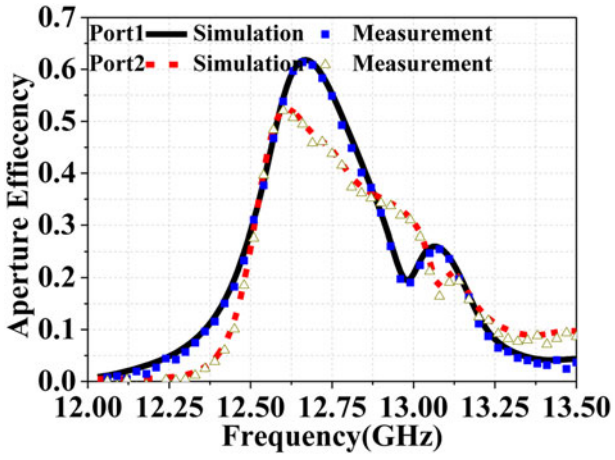

Fig. 14. Aperture efficiencies of proposed antenna for port1 and port2.

substrate to feed the antenna. Here, note that two off-centered slots working on different *S*11 bands radiating HLP and VLP waves cause a slight difference in CP properties, although they are transmitted throughout the only RT-MS superstation. Particularly, the two non-uniform located slots affect the radiating LP wave's characteristics, such as the angle and distances to MSs, more than when hitting on MSs. Thus, the response of the polarization properties resulting from the angle and distances of the radiated waves is slightly different, making the results of LHCP and RHCP different. Then, we can conclude that slight variations occur in the coming results, but have little effect on the correctness of the design.

The PCM forms the top layer as a superstrate, separated from Sub #3 by an air gap, h_C, to form an FP resonant cavity enabled by gain improvement. The separation height, h_c, can be calculated by (1) and adjusted by simulations through HFSS to get an optimum value. In this design, considering its wideband and stable broadside radiation, a double *H*-shaped slot etched in the ground plane is unitized to an energy coupling for size reduction. Two orthogonal feed lines are adopted to feed the slots to excite two perpendicular linear polarization modes. Through numerous simulations, analyses, and comparisons, we obtained the optimal dimensions (Table 1).

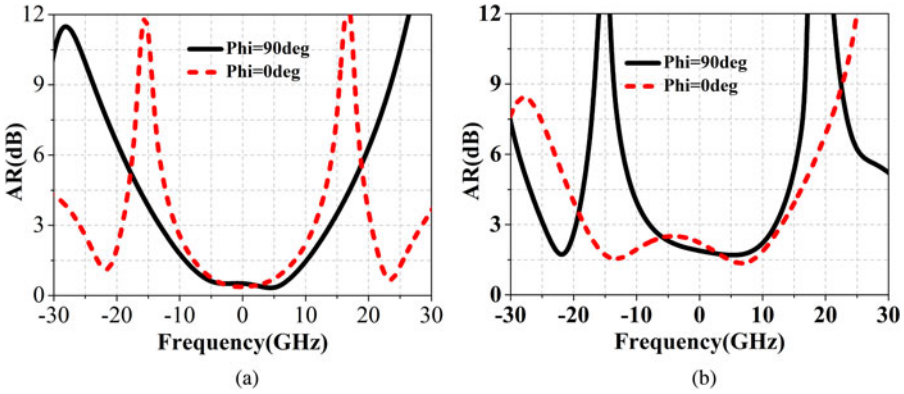

Fig. 13. Simulated ARs versus incident angle fed by port1 and port2, at 12.5 and 12.6 GHz, respectively.

https://doi.org/10.1017/S1759078722001027 Published online by Cambridge University Press

https://doi.org/10.1017/S1759078722001027 Published online by Cambridge University Press

Table 2. Performance comparison of the recently reported CP-FP antennas

Ref.	Size (λ_0^3)	Method	3 dB AR BW (GHz)	Isolation (dB)	Peak gain (dBic)	Aperture efficiency (%)	High-gain method	Operating bandwidth (GHz)
Proposed	**2.6 × 2.6 × 0.78**	**Dual feed**	**12.21–13.1 (LHCP)12.35–13.1 (RHCP)**	**>25**	**16.5 (LHCP)15.97 (RHCP)**	**63.254.6**	**FP cavity**	**12.2–13.28 12.5–13.5**
[1]	2.0 × 2.0 × 0.45	Feed network	8.1–10.0 (LHCP)	–	11.2	25.6	FP cavity	8.25–9.5
[16]	2.20 × 2.20 × 0.8	Single feed	2.51–2.56	>15	13.3	–	FP cavity	2.49–2.52
[25]	2.0 × 2.0 × 0.6	Reconfiguration feed	7.3–7.6 (LHCP and RHCP)	–	15.1	42.3	FP cavity	7.3–7.6
[26]	2.6 × 2.63 × 0.36	Dual feed	2.8% (LHCP and RHCP)	>15	13.4 (LHCP and RHCP)	24.5	FP cavity	9.86–10.14
[27]	2.5 × 2.5 × 1.4	Dual feed	12.07–13.68 (LHCP) 12.16–13.74 (RHCP)	>25	12.78 (LHCP) 12.89 (RHCP)	–	FP cavity	11.58–13.25 11.73–13.8
[33]	3.0 × 3.0 × 0.36	Single feed	9.8–10.2 (RHCP)	–	17.8 (RHCP)	53.3	FP cavity	9.8–10.2
[34]	14 × 20 × 0.16	Feed network	54.2–64.3 (LHCP) 54.8–65 (RHCP)	–	13.7 (LHCP) 17.85 (RHCP)	–	Array	55–66
[35]	2.1 × 2.1 × 0.03	Dual feed	9.66–10.66 (LHCP and RHCP)	>15	13.5	–	Array	9.75–10.3 9.75–10.3
[36]	4.3 × 4.3 × 0.7	Feeding network	26.8–33.1	–	20	41.7	FP cavity	26.7–34.2
[37]	1.75 × 1.75 × 0.78	Single feed	12.4–16.8	–	11.45	36.3	FP cavity	11.7–19.8
[38]	2.13 × 2.13 × 0.69	Single feed	8.5–11.5	–	14.7	51.3	FP cavity	8.3–11.6
[39]	2.0 × 2.0 × 0.88	Single feed	4.12–6.39	–	14.5	56.1	FP cavity	3.82–6.01

Note: "–" represents null.

Simulated and measured results

To validate the performance of the proposed antenna simulated by HFSS, we fabricated a prototype antenna, as displayed in Fig. 8, and measured it in an anechoic chamber using a far-field testing system. The measurements of the near-field data, *S*11, were completed by a vector network analyzer. Figures 9(a) and 9(c) show the plots of simulated and measured reflection coefficients for the two ports. It can be seen that an impedance bandwidth, determined by $S11 < -10$ dB, of 12.2–13.28 and 12.5–13.5 GHz, about 7.28 and 15.38%, respectively, is achieved for port1 and port2, respectively, which agrees well with the measured results except for some reasonable error. The antenna has the measured 3 dB axial ratios (ARs) for the two ports of 12.21–13.1 GHz (7.03%) and 12.35–13.1 GHz (5.89%), respectively, almost falling into the corresponding impedance bandwidths, as shown in Fig. 9(b). It also has minimum AR values of 0.3 and 1 dB, respectively, for port1 and port2, respectively, which validates the excellent CP characteristics.

The measured peak gain for LHCP and RHCP radiation can reach 16.3 and 15.97 dBic at 12.58 and 12.7 GHz, respectively, so there is little difference between them. Moreover, both have a gain that is 11 dBic higher than that of the feeding antenna. To our knowledge, this is the highest gain of dual-circularly polarization of such compact size, of $2.6\lambda_0 \times 2.6\lambda_0$, as depicted in Figs 9(b) and 9(d). Then, a slight difference occurs, mainly owing to measurement errors and machining accuracy, but it does not affect the design correctness. The isolation of the two ports within the impedance bandwidths is plotted in Fig. 9(e), and both have a gain of less than −25 dB.

Another important radiation parameter, the radiation pattern, was investigated, as shown in Figs 10 and 11. Figures 10(a) and 10(b) show the LHCP wave radiation pattern at 13.5 GHz in the *xoz* and *yoz* plane, respectively, and Figs 11(a) and 11(b) show the RHCP wave radiation pattern in the *xoz* and *yoz* planes, which are apparently fed by port1 and port2, respectively. The figure confirms that the dual-polarization radiated wave into space passes through the designed PCM. From this, it can be seen that both side lode levels are less than −10 dB, and the cross-polarization levels are less than −15 dB. The measured results match well with the simulation results, suggesting excellent radiation performance.

Figure 12 demonstrates that the radiation efficiency of the designed antenna, whether fed by port1 or port2, can be a maximum of more than 0.85 and a minimum of more than 0.8 in the working band, except there is a small degeneration of 0.05 in RHCP radiation fed by port2.

Figure 13 shows the AR value versus the angle in the *xoz* and *yoz* planes at 12.6 GHz. We can see that exceeding 20° of an AR value of lower than 3 dB in the main beam can be achieved, suggesting better CP radiation. The aperture efficiencies of the designed antenna for LHCP and RHCP radiation are displayed in Fig. 14, suggesting that maximum points of 63.2 and 54.6% occur at 12.58 and 12.7 GHz, respectively, indicating higher aperture efficiency compared with recent work.

As listed in Table 2, compared with recently reported FP-CP antennas, the designed antenna can realize high gain, wideband dual-CP radiation with a more compact size and a simpler structure. By adopting a double slot with a cross arrangement, the proposed antenna can achieve independently controlled radiation, making it more flexible and possible to realize a high gain than other reported antennas.

Conclusions

We have presented a RT-MS-based FP resonant antenna with dual-CP. The RT-MS consists of three metal substrates, a rectangular patch at the bottom, as a receiver; a coupling cross-slot in the middle; and a corner-cut patch at the top, as a transmitter. Owing to the high reflectivity and aperture efficiency generated by the cross-slot, and by adopting an independently controlled dual-LP source antenna as the feeder and 12×12 cells arranged RT-MS array as the superstrate, the antenna has been shown to achieve better results in the gain property, wideband, and wide 3 dB axial ratio than other similar FP antennas. The proposed antenna has been fabricated and measured, and has shown a reasonable agreement except for slight errors with simulations. The results verify the correctness of our design. For the working band falling into the X/Ku band, it has achieved a high gain. Thus, the proposed antenna can be applied to army and commercial communications and other high-sensitivity applications for polarization wireless communications systems.

References

1. **Li K, Liu Y, Jia Y and Guo YJ** (2017) A circularly polarized high gain antenna with low RCS over a wideband using chessboard polarization conversion metasurfaces. *IEEE Transactions on Antennas and Propagation* **65**, 4288–4292.
2. **Huang Y, Yang L, Li J, Wang Y and Wen G** (2016) Polarization conversion of metasurface for the application of wide band low-profile circular polarization slot antenna. *Applied Physics Letters* **109**, 054101.
3. **Wu Z, Li L, Li Y and Chen X** (2015) Metasurface superstrate antenna with wideband circular polarization for satellite communication application. *IEEE Antennas and Wireless Propagation Letters* **10**, 907–910.
4. **Zhu HL, Cheung SW, Chung KL and Yuk TI** (2013) Linear-to-circular polarization conversion using metasurface. *IEEE Transactions on Antennas and Propagation* **61**, 4615–4623.
5. **Liu ZG, Cao ZX and Wu LN** (2016) Compact low-profile circularly polarized Fabry-Perot resonator antenna fed by linearly microstrip patch. *IEEE Antennas and Wireless Propagation Letters* **16**, 524–527.
6. **Chen Q and Zhang H** (2018) Dual-patch polarization conversion metasurface-based wideband circular polarization slot antenna. *IEEE Access* **6**, 74772–74777.
7. **Chen Q and Zhang H** (2019) High-gain circularly polarized Fabry-Pérot patch array antenna with wideband low-radar-cross-section property. *IEEE Access* **7**, 8885–8889.
8. **Lin C, Ge Y, Bird TS and Liu K** (2018) Circularly-polarized horns based on standard horns and a metasurface polarizer. *IEEE Antennas and Wireless Propagation Letters* **17**, 480–484.
9. **Xie P, Wang G, Li H and Liang J** (2017) A dual-polarized two-dimensional beam-steering Fabry-Perot cavity antenna with a reconfigurable partially reflecting surface. *IEEE Antennas and Wireless Propagation Letters* **16**, 2370–2374.
10. **Zeb BA and Esselle KP** (2015) High-gain dual-band dual-polarised electromagnetic band gap resonator antenna with an all-dielectric superstructure. *IET Microwaves, Antennas & Propagation* **9**, 1059–1065.
11. **Cai Y, Li K, Li W, Gao S, Yin Y, Zhao L and Hu W** (2020) Dual-band circularly polarized transmitarray with single linearly polarized feed. *IEEE Transactions on Antennas and Propagation* **68**, 5015–5020.
12. **Qin F, Gao S, Wei G, Luo Q, Mao C, Gu C, Xu J and Li J** (2015) Wideband circularly polarized Fabry-Perot antenna [antenna applications corner]. *IEEE Antennas and Propagation Magazine* **57**, 127–135.
13. **Cheng Y and Dong Y** (2020) Bandwidth enhanced circularly polarized Fabry-Perot cavity antenna using metal strips. *IEEE Access* **8**, 60189–60198.
14. **Hussain N, Naqvi SI, Awan WA and Le TT** (2020) A metasurface-based wideband bidirectional same sense circularly polarized antenna. *International Journal of RF and Microwave Computer-Aided Engineering* **30**, e22262.

https://doi.org/10.1017/S1759078722001027 Published online by Cambridge University Press

15. **Hussain N, Jeong M, Park J and Kim N** (2019) A broadband circularly polarized Fabry-Perot resonant antenna using a single-layered PRS for 5G MIMO applications. *IEEE Access* **7**, 42897–42907.
16. **Muhammad SA, Sauleau R, Le Coq L and Legay H** (2011) Self-generation of circular polarization using compact Fabry-Perot cavity antennas. *IEEE Antennas and Wireless Propagation Letters* **10**, 907–910.
17. **Liu ZG and Lu WB** (2017) Low-profile design of broadband high gain circularly polarized Fabry-Perot resonator antenna and its array with linearly polarized feed. *IEEE Access* **5**, 7164–7172.
18. **Ji L, Qin P, Jay Guo Y, Ding C, Fu G and Gong S** (2016) A wideband polarization reconfigurable antenna with partially reflective surface. *IEEE Transactions on Antennas and Propagation* **64**, 4534–4538.
19. **Naseri P and Hum SV** (2019) A dual-band dual-circularly polarized reflectarray for K/Ka-band space applications. *2019 13th European Conference on Antennas and Propagation (EuCAP), Krakow, Poland*, pp. 1–5.
20. **Chen W, Yu Z, Zhai J and Zhou J** (2020) Developing wideband dual-circularly polarized antenna with simple feeds using magnetoelectric dipoles. *IEEE Antennas and Wireless Propagation Letters* **19**, 1037–1041.
21. **Singh DK, Kanaujia BK, Dwari S and Pandey GP** (2020) Modeling of a dual circularly polarized capacitive-coupled slit-loaded truncated microstrip antenna. *Journal of Computational Electronics* **19**, 1564–1572.
22. **Naseri P, Costa JR, Matos SA, Fernandes CA and Hum SV** (2020) Equivalent circuit modeling to design a dual-band dual linear-to-circular polarizer surface. *IEEE Transactions on Antennas and Propagation* **68**, 5730–5735.
23. **Guo W, Wang G, Ji W, Zheng Y, Chen K and Feng Y** (2020) Broadband spin-decoupled metasurface for dual-circularly polarized reflector antenna design. *IEEE Transactions on Antennas and Propagation* **68**, 3534–3543.
24. **Jiang Z, Zhang Y and Hong W** (2020) Anisotropic impedance surface enabled low-profile broadband dual circularly-polarized multi-beam reflect-arrays for Ka-band applications. *IEEE Transactions on Antennas and Propagation* **68**, 6441–6446.
25. **Tran HH and Park HC** (2020) A simple design of polarization reconfigurable Fabry-Perot resonator antenna. *IEEE Access* **8**, 91837–91842.
26. **Wang Y and Zhang A** (2021) Dual circularly polarized Fabry Perot resonator antenna employing a polarization conversion metasurface. *IEEE Access* **99**, 1.
27. **Huang R, Wang Z, Li G, Lin C, Ge Y and Pu J** (2021) A metasurface-enabled wideband high-gain dual-circularly-polarized Fabry-Perot resonator antenna. *Microwave and Optical Technology Letters* **9**, 44881–44887.
28. **Pan W, Huang C, Ma X, Jiang B and Luo X** (2015) A dual linearly-polarized transmitarray element with 1-bit phase resolution in X-band. *IEEE Transactions on Antennas and Propagation* **60**, 167–170.
29. **Clemente A, Dussopt L, Sauleau R, Potier P and Pouliguen P** (2012) 1-bit reconfigurable unit cell based on PIN diodes for transmit-array applications in X-band. *IEEE Transactions on Antennas and Propagation* **60**, 2260–2269.
30. **Baena JD, Glybovski SB, del Risco JP, Slobozhanyuk AP and Belov PA** (2017) Broadband and thin linear-to-circular polarizers based on self-complementary zigzag metasurfaces. *IEEE Transactions on Antennas and Propagation* **59**, 2513–2523.
31. **Diaby F, Clemente A, Pham KT, Sauleau R and Dussopt L** (2018) Circularly-polarized transmitarray antennas at Ka-band. *IEEE Antennas and Wireless Propagation Letters* **14**, 108–111.
32. **Xie P, Wang G, Li H, Liang J and Gao X** (2020) Circularly polarized Fabry-Perot antenna employing a receiver-transmitter polarization conversion metasurface. *IEEE Transactions on Antennas and Propagation* **68**, 3213–3218.
33. **Xie P, Wang G, Zong B and Zou X** (2021) A novel receiver-transmitter metasurface for a high-aperture-efficiency Fabry-Perot resonator antenna. *China Physical B* **30**, 6.
34. **Zhu J, Liao S, Yang Y, Li S and Xue Q** (2018) 60 GHz dual-circularly polarized planar aperture antenna and array. *IEEE Transactions on Antennas and Propagation* **66**, 1014–1019.
35. **Chen SJ and Fumeaux C** (2017) Dual circularly polarized series-fed microstrip patch array with coplanar proximity coupling. *IEEE Antennas and Wireless Propagation Letters* **16**, 1500–1503.
36. **Zheng Y, Gao J, Zhou Y, Cao X, Yang H, Li S and Li T** (2018) Wideband gain enhancement and RCS reduction of Fabry-Perot resonator antenna with chessboard arranged metamaterial superstrate. *IEEE Transactions on Antennas and Propagation* **66**, 590–599.
37. **Chen L, Chang L, Chen Z and Qiu Q** (2020) Bandwidth-enhanced circularly polarized spiral antenna with compact size. *IEEE Access* **8**, 41246–41253.
38. **Kabiri S, Kornaros E and Flaviis FD** (2019) Wideband circular polarized Fabry-Perot cavity antennas for V-band indoor point-to-point communications. *Electromagnetics* **39**, 198–216.
39. **Ge Y and Qin K** (2018) Wideband high-gain circularly polarized Fabry-Perot antenna feeding a conical short-horn. *International Journal of RF and Microwave Computer-Aided Engineering* **28**, e21430.

Zhiqiang Yuan was born in Jiangxi, China. He received the B.S. and M.S. degrees from Wuhan University of Technology, Wuhan, China, in 2005 and 2011, respectively. His research interests include wireless communication and network.

https://doi.org/10.1017/S1759078722001027 Published online by Cambridge University Press